

3D modelling of macroscopic force-free effects in superconducting thin films and rectangular prisms.

M. Kapolka, E. Pardo

Institute of Electrical Engineering, Slovak Academy of Sciences,

Dubravska 9, 84104 Bratislava, Slovakia

(Dated: July 23, 2019)

When the magnetic field has a parallel component to the current density \mathbf{J} there appear force-free effects due to flux cutting and crossing. This results in an anisotropic $\mathbf{E}(\mathbf{J})$ relation, being \mathbf{E} the electric field. Understanding force-free effects is interesting not only for the design of superconducting power and magnet applications but also for material characterization.

This work develops and applies a fast and accurate computer modeling method based on a variational approach that can handle force-free anisotropic $\mathbf{E}(\mathbf{J})$ relations and perform fully three dimensional (3D) calculations. We present a systematic study of force-free effects in rectangular thin films and prisms with several finite thicknesses under applied magnetic fields with arbitrary angle θ with the surface. The results are compared with the same situation with isotropic $\mathbf{E}(\mathbf{J})$ relation.

The thin film situation shows gradual critical current density penetration and a general increase of the magnitude of the magnetization with the angle θ but a minimum at the remnant state of the magnetization loop. The prism model presents current paths with 3D bending for all angles θ . The average current density over the thickness agrees very well with the thin film model except for the highest angles. The prism hysteresis loops reveal a peak after the remnant state, which is due to the parallel component of the self-magnetic-field and is implicitly neglected for thin films.

The presented numerical method shows the capability to take force-free situations into account for general 3D situations with a high number of degrees of freedom. The results reveal new features of force-free effects in thin films and prisms.

I. INTRODUCTION

Type II superconductors are essential for large bore or high-field magnets [1–4] and are promising for power applications, such as motors for air-plane [5, 6] or ship propulsion [7, 8], generators [9–11], grid power-transmission cables [12, 13], transformers [14–17], and or fault-current limiters [18–22]. The Critical Current Density, J_c , of type II superconductors depends on the magnitude and angle of the local magnetic field. There are three types of anisotropy which we call “intrinsic”, “de-pinning”, and “force free” anisotropy.

The “intrinsic” anisotropy is the following. Certain superconductors present an axis with suppressed superconductivity, where the critical current density is lower. In cuprates, for instance, the critical current density in the c crystallographic axis is much smaller than in the ab plane. There is also important anisotropy in REBCO vicinal films due to flux channeling [23, 24].

The “de-pinning” anisotropy of J_c is due to anisotropic maximum pinning forces caused by either anisotropic pinning centres or anisotropic vortex cores [25]. When the current density \mathbf{J} is perpendicular to \mathbf{B} and the electric field \mathbf{E} is parallel to \mathbf{J} , the anisotropy of J_c is always due to de-pinning anisotropy. This kind of anisotropy is important for High-Temperature Superconductors (HTS), such as $(\text{Bi,Pb})_2\text{Sr}_2\text{Ca}_2\text{Cu}_3\text{O}_{10}$ and $\text{REBa}_2\text{Cu}_3\text{O}_{7-x}$, and iron-based superconductors. The magnetic field dependence and anisotropy has an impact on the performance of magnets and power applications.

Another type of anisotropy is the “force-free” anisotropy, which appears when the current density presents a substantial parallel component with the local magnetic field. The parallel \mathbf{J} component does not contribute to the macroscopic driving force (or Lorentz force) on the vortices, $\mathbf{F} = \mathbf{J} \times \mathbf{B}$, being the microscopic vortex dynamics for $\mathbf{B} \parallel \mathbf{J}$ a complex process that includes flux cutting and crossing [26–28]. Many power applications with rotating applied fields are influenced with force-free effects. In principle, the force-free anisotropy also appears for intrinsically isotropic materials.

There are many macroscopical physical models on force-free anisotropy that regard both flux cutting and de-pinning, such as the Double Critical State Model [27], the General Double Critical State Model [29], Brant and Mikitik Extended Double Critical State Model [30] and the Elliptic Critical State Model [31]. A valuable comparison of these models can be found in [28]. There are many experimental works on de-pinning anisotropy, such as state of the art

REBCO commercial tapes [32–38], Bi2223 tapes [39, 40] and iron based [41–44] conductors, as well as a database of anisotropic J_c measurements [45]. Correction of self-magnetic field in critical current, I_c , measurements is also important [46, 47].

In this article, we focus on force-free effects, which cause anisotropy when \mathbf{J} has a parallel component to \mathbf{B} (or \mathbf{E} is not parallel to \mathbf{J}). We also base our study in modelling only. The object of study are thin films and rectangular prisms of several thickness with various angles of the applied fields, with a especial focus on the current path and hysteresis loops. We compared results with the isotropic situation, in order to understand the observed behavior. The modelling is performed by Minimum Electro-Magnetic Entropy Production in 3D [48], which is suitable for 3D calculations, and avoids spending variables in the air. Moreover, the method enables force-free anisotropic power laws [49], which is the core of this study.

II. MATHEMATICAL MODEL

A. MEMEP 3D method

This study is based on the Minimum ElectroMagnetic Entropy Production in 3D (MEMEP 3D) [48], which is a variational method. The method solves the effective magnetization \mathbf{T} , defined as

$$\nabla \times \mathbf{T} = \mathbf{J}, \quad (1)$$

where \mathbf{J} is the current density. In addition to the magnetization case, MEMEP 3D can also take transport currents into account, after adding an extra term in (1) (see [48]). We take the interpretation that \mathbf{T} is an effective magnetization due to the screening currents. The \mathbf{T} vector is non-zero only inside the sample, and hence the method avoids discretization of the air around the sample. The advantages of MEMEP 3D are reduction of computing time, enabling an increase of total number of degrees of freedom in the sample volume, and efficient parallelization. The general equation of electric field \mathbf{E} is derived from Maxwell equations

$$\mathbf{E}(\mathbf{J}) = -\dot{\mathbf{A}} - \nabla\phi, \quad (2)$$

$$\nabla \cdot \mathbf{J} = 0, \quad (3)$$

where ϕ is the scalar potential.

In the Coulomb's gauge, we can split the vector potential \mathbf{A} to \mathbf{A}_a and \mathbf{A}_J , where \mathbf{A}_a is the vector potential contributed by the applied field and \mathbf{A}_J is the vector potential contributed by the current density inside the sample. Then, \mathbf{A}_J is

$$\mathbf{A}_J(\mathbf{r}) = \frac{\mu_0}{4\pi} \int_V d^3\mathbf{r}' \frac{\mathbf{J}(\mathbf{r}')}{|\mathbf{r} - \mathbf{r}'|} = \frac{\mu_0}{4\pi} \int_V d^3\mathbf{r}' \frac{\nabla' \times \mathbf{T}(\mathbf{r}')}{|\mathbf{r} - \mathbf{r}'|}, \quad (4)$$

where \mathbf{r} and \mathbf{r}' are position vectors.

According to the definition of \mathbf{T} , we can rewrite equations (2) and (3) into

$$\mathbf{E}(\nabla \times \mathbf{T}) = -\dot{\mathbf{A}} - \nabla\phi, \quad (5)$$

$$\nabla \cdot (\nabla \times \mathbf{T}) = 0. \quad (6)$$

The second equation is always satisfied, and hence we must solve only the first equation. As it was shown in [48], minimizing the following functional, is the same as solving equation (5).

The functional is

$$L_T = \int_V d^3\mathbf{r} \left[\frac{1}{2} \frac{\Delta\mathbf{A}_J}{\Delta t} \cdot (\nabla \times \Delta\mathbf{T}) + \frac{\Delta\mathbf{A}_a}{\Delta t} \cdot (\nabla \times \Delta\mathbf{T}) + U(\nabla \times \mathbf{T}) \right], \quad (7)$$

where U is the dissipation factor, defined as

$$U(\mathbf{J}) = \int_0^J \mathbf{E}(\mathbf{J}') \cdot d\mathbf{J}'. \quad (8)$$

The functional can include any $\mathbf{E}(\mathbf{J})$ relation with its corresponding dissipation factor. The functional is solved in the time domain in time steps like $t = t_0 + \Delta t$, where t is the present time, t_0 is the previous time step and Δt is the time between two time steps. The magnetic moment \mathbf{m} is calculated by equation

$$\mathbf{m} = \frac{1}{2} \int d^3\mathbf{r} \mathbf{J} \times \mathbf{r}, \quad (9)$$

where \mathbf{r} is a position vector of interpolated \mathbf{J} at the centre of the cell. The magnetization is $\mathbf{M} = \mathbf{m}/V$ and V is volume of the sample. Then, we define $\mathbf{T}, \mathbf{A}_J, \mathbf{A}_a$ as the value of the corresponding variables at the present time step; $\Delta\mathbf{T}, \Delta\mathbf{A}_J, \Delta\mathbf{A}_a$ are the change of the variables between two time steps; and $\mathbf{T}_0, \mathbf{A}_{J0}, \mathbf{A}_{a0}$ are the variables from the previous time step. In this work, the applied magnetic field \mathbf{B}_a is uniform and Δt is constant, although the method enables non-uniform \mathbf{B}_a and variable Δt .

B. $\mathbf{E}(\mathbf{J})$ relation

In a previous study [50], we used the isotropic power law as $\mathbf{E}(\mathbf{J})$ relation in the functional (7)

$$\mathbf{E}(\mathbf{J}) = E_c \left(\frac{|\mathbf{J}|}{J_c} \right)^n \frac{\mathbf{J}}{|\mathbf{J}|}, \quad (10)$$

where $\mathbf{B} \perp \mathbf{J}$, $\mathbf{E} \parallel \mathbf{J}$, and E_c is the critical electric field 10^{-4} V/m, J_c is the critical current density, and n is the power law exponent or n factor. The n factor depends on the quality of the superconducting materials, temperature and local magnetic field \mathbf{B} . The Bean Critical State Model (CSM)[51, 52] corresponds to $n \rightarrow \infty$, but real superconductors present smaller n factors, ranging from around 10 to the order of 100. The case of $n=100$ is practically equivalent to the CSM. The dissipation factor for isotropic $\mathbf{E}(\mathbf{J})$ relation of (10) is

$$U(\mathbf{J}) = \frac{E_c J_c}{n+1} \left(\frac{|\mathbf{J}|}{J_c} \right)^{n+1}. \quad (11)$$

In this article, we focus on the anisotropic case, in order to model the force-free effects with anisotropic power law [49].

$$\mathbf{E}(\mathbf{J}) = 2m_0 U_0 \left[\left(\frac{J_{\parallel}}{J_{c\parallel}} \right)^2 + \left(\frac{J_{\perp}}{J_{c\perp}} \right)^2 \right]^{m_0-1} \cdot \left(\frac{J_{\parallel}}{J_{c\parallel}^2} \mathbf{e}_{\parallel} + \frac{J_{\perp}}{J_{c\perp}^2} \mathbf{e}_{\perp} \right), \quad (12)$$

where $m_0 = (n+1)/2$, $U_0 = E_c J_{c\perp}/(n+1)$, $J_{\parallel} = \mathbf{J} \cdot \mathbf{B}/|\mathbf{B}|$, $J_{\perp} = |\mathbf{J} \times \mathbf{B}|/|\mathbf{B}|$, and $J_{c\perp}$ and $J_{c\parallel}$ are critical current densities parallel and perpendicular to \mathbf{B} , respectively. Vector \mathbf{B} is the local magnetic field and \mathbf{e}_{\perp} , \mathbf{e}_{\parallel} are unit vectors of the current density, where $\mathbf{e}_{\parallel} = \mathbf{B}/|\mathbf{B}|$, $\mathbf{e}_{\perp} = \mathbf{J}_{\perp}/|\mathbf{J}_{\perp}|$ and $\mathbf{J}_{\perp} = \mathbf{J} - J_{\parallel} \mathbf{e}_{\parallel}$. Notice that $\mathbf{J} = J_{\parallel} \mathbf{e}_{\parallel} + J_{\perp} \mathbf{e}_{\perp}$ and J_{\perp} is always positive. The applied magnetic field \mathbf{B}_a is not always perpendicular to the sample surface [figure 3 (a)]. The corresponding anisotropic dissipation factor is

$$U(\mathbf{J}, \mathbf{B}) = U_0 \left[\left(\frac{J_{\parallel}}{J_{c\parallel}} \right)^2 + \left(\frac{J_{\perp}}{J_{c\perp}} \right)^2 \right]^{m_0}. \quad (13)$$

The anisotropic power law becomes the elliptic CSM for large enough m_0 or n with two critical current densities $J_{c\perp}$, $J_{c\parallel}$, which apply according to direction of the local magnetic field \mathbf{B} . The problem of the anisotropic $U(\mathbf{J}, \mathbf{B})$ relation is the uncertainty of the unit vector of local magnetic field \mathbf{B} with very low or zero $|\mathbf{B}|$. In the samples there exist places where

the local magnetic field vanishes. We suggest the following two options in order to remove this uncertainty.

The first option is to use a sharp $J_{c\perp}(\mathbf{B})$ and $J_{c\parallel}(\mathbf{B})$ dependence, where at $|\mathbf{B}| \rightarrow \infty$ they follow $J_{c\parallel} \neq J_{c\perp}$ and at $|\mathbf{B}| = 0$, $J_{c\parallel} = J_{c\perp} \equiv J_{c0}$ with a linear transition between $|\mathbf{B}| = 0$ and a certain magnetic field $|\mathbf{B}| = B_s$, being B_s a small magnetic field [figure 1(a)]. The limit of $B_s \rightarrow 0$ corresponds to the elliptic critical state model [53]. For simplicity, we consider only this linear dependence of B for $J_{c\parallel}$, keeping $J_{c\perp}$ as constant. The reason is to reproduce the Bean CSM for perpendicular applied fields.

The magnetic field is calculated from the current density after the functional is minimized. The functional is solved iteratively [48]: at the first iteration, \mathbf{T} is calculated with $\mathbf{B}_J = \mathbf{B}_{J0}$ and $\mathbf{B}_a \neq 0$, being \mathbf{B}_{J0} the magnetic field generated by \mathbf{J} at the previous time step, the second iteration starts with $\mathbf{B}_J \neq 0$ calculated from \mathbf{J} at the previous iteration, where $\mathbf{J} = \nabla \times \mathbf{T}$; iterations are repeated until we find a solution with given tolerance in each component of \mathbf{J} . The sharp $J_{c\parallel}(B)$ dependence causes numerical problems in this iterative method, since a small error in \mathbf{B} causes a large error in \mathbf{J} in the next iteration step.

In order to avoid this numerical problem, the functional is minimized in a certain time t with the total magnetic field \mathbf{B} from the previous time step $\mathbf{B}(t - \Delta t)$. The vector potential \mathbf{A} is still calculated according the present time t . This is the reason why the remanent state is shifted by Δt in the results. The negative effect of that assumption can be decreased by increasing the number of time steps in one period of applied magnetic field.

Another option to avoid the problems at $|\mathbf{B}| \rightarrow 0$ is to assume Kim's model for both $J_{c\parallel}(B)$ and $J_{c\perp}(B)$ dependences, where $J_{c\parallel}(B = 0) = J_{c\perp}(B = 0) \equiv J_{c0}$ and $J_{c\parallel} \neq J_{c\perp}$ for $\mathbf{B} \rightarrow \infty$ [figure 1(b)]. This Kim model is

$$J_{c\parallel}(B) = \frac{J_{c0}}{\left(1 + \frac{|\mathbf{B}|}{B_{0\parallel}}\right)^m}, \quad (14)$$

$$J_{c\perp}(B) = \frac{J_{c0}}{\left(1 + \frac{|\mathbf{B}|}{B_{0\perp}}\right)^m}, \quad (15)$$

where in this article we choose $m=0.5$, $B_{0\perp}=20$ mT, $J_{c0} = 3 \cdot 10^{10}$ A/mm² and $B_{0\parallel} = 9B_{c\perp}$, so that $J_{c\parallel}(B \rightarrow \infty) = 3J_{c\perp}(B \rightarrow \infty)$. For this case, the $J_{c\parallel}(B)$ and $J_{c\perp}(B)$ dependences are not sharp, and hence we use the original iterative method for magnetic field dependent J_c . Then, \mathbf{J} at time t uses \mathbf{B} of the same time t . Moreover, this smooth $J_{c\perp}(B), J_{c\parallel}(B)$

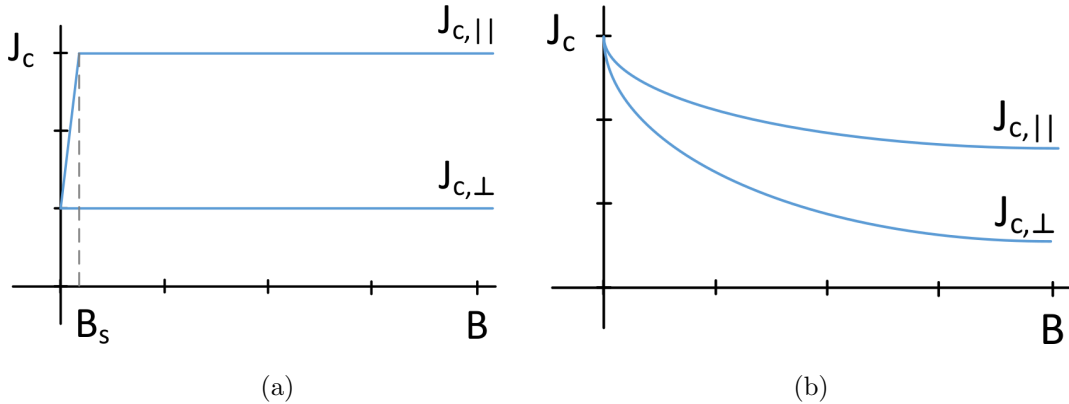


FIG. 1: Using a magnetic field dependence for $J_{c||}$ and $J_{c\perp}$ avoids indeterminations at $\mathbf{B} = 0$. (a) Elliptic double critical-state model (CSM). (b) Anisotropic Kim model.

dependence is more realistic than the elliptical CSM.

C. Sector minimization

Reduction of computing time is of essential importance for 3D calculations. We already studied the case of parallel minimization by sectors, where sectors are overlapping by one cell [48]. In this article, we increase the overlapping of sectors in the following way. Now, the sectors are not overlapping to each other, and hence they share only the edge on the border, which are not solved (figure 2(a)). Then, we added other 2 sets of sectors, but the boundary in each set of sectors is shifted along the diagonal by $1/3$ of the sector-diagonal size (figure 2(b,c)). The edge in the boundary in the first set is solved at least once in some of the other two sets. The additional sets increase the memory usage, which is still low, but they decrease the computing time. Sets of the sectors are minimized in series one after the other, but sectors within each set are solved in parallel to achieve high efficiency of parallel computing. Although computing all three sets of sectors in parallel could further enhance parallelization, we have found that solving each set sequentially reduces computing time. The process of solving all 3 sets subsequently is repeated until the maximum difference in any component of \mathbf{T} between two iterations of the same set is below a certain tolerance. We use elongated cells, in order to improve the accuracy for a given number of cells, as detailed in appendix A.

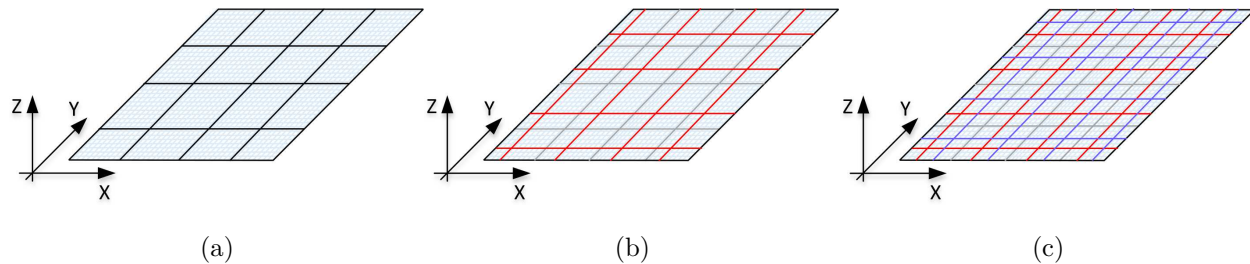


FIG. 2: Using three sets of sectors speeds up the calculations. (a) Boundaries of the first set only. (b) First and second set. (c) All three sets.

III. RESULTS AND DISCUSSION

As a result of the variational model, we calculated two geometries like an infinitesimally thin film (or simply, “thin film”) and a thin prism with finite thickness (or “thin prism”) [figure 3 (a),(b)]. The force-free effects are modelled with the anisotropic power-law in combination of either constant $J_{c\perp}$, $J_{c\parallel}$ or Kim model $J_{c\perp}(B)$, $J_{c\parallel}(B)$. We calculated as well the pure isotropic case of a thin film and thin prism for comparison. The calculations are performed with two values of the n -factor, 30 and 100, in order to have results close to the realistic values and analytical critical-state formulas, respectively.

A. Anisotropic force-free effects in films

In this section, we study square thin films of dimensions $12 \times 12 \text{ mm}^2$ and thickness $1 \mu\text{m}$. We also take the common assumption of the thin film limit, which consists on averaging the electromagnetic properties over the sample thickness. For our method, this is achieved by taking only one cell along the sample thickness. We used a total number of degrees of freedom of 4200.

1. Power device situation

In this section, the magnetic applied field \mathbf{B}_a has a sinusoidal waveform of 50 Hz and the same perpendicular, $B_{a,z}$, component for all angles θ with amplitude $B_{a,z,m} = 50 \text{ mT}$ [figure 3(a)]. The angle $\theta = 0^\circ$ is completely perpendicular to the surface of the thin film. We calculated the cases with $\theta = 0^\circ, 45^\circ, 60^\circ, 80^\circ$. For this study, the perpendicular critical

current density $J_{c\perp}$ is equal to $3 \cdot 10^{10}$ A/m² and $J_{c\parallel}$ is 3 times higher. The dependence of J_c on the magnetic field is on figure 1(a), where we choose $B_s = 1$ mT. The n factor of the anisotropic power law is equal 30, which is a realistic value for REBCO tapes in self-field.

The first case, with $\theta = 0^\circ$, is shown on figure 4. The penetration of the current density to the film strip is explained by colour maps of $|\mathbf{J}|$ normalized to $J_{c\perp}$, while the lines are current flux lines. The current density gradually penetrates to the sample after increasing the applied field [figure 4(a)], until it reaches almost saturated state at the peak of applied field [figure 4(b)]. During the decrease of the applied field, current starts penetrating again from the edges of the sample with opposite sign till the centre. The quasi remanent state, at $B_a \approx 0$ mT, presents symmetric penetration of \mathbf{J} along both x and y axis [figure 4(c)]. We show the first time step after remanence, $\mathbf{B} = 0$, for comparison with the cases with $\theta \neq 0^\circ$, where we use \mathbf{B} of the previous time step in order to obtain $J_{c\parallel}$ [figure 4(a)].

The second case is for $\theta = 45^\circ$ and applied field amplitude $B_{am} = 70.7$ mT (figure 5). The force-free effects appear during the increase of the applied field [figure 5(a)]. The current lines parallel to the x axis are more aligned with the direction of the applied field. Therefore, $J_{c\parallel}$ becomes relevant, and hence current density at that direction is higher compared to the current density along the y axis. The current penetration depth is smaller from top and bottom at the peak [figure 5(b)] compared to that from the sides. The penetration depth of J_y from right and left is the same as for $\theta = 0^\circ$, because J_y is still perpendicular to B_a . The quasi remanent state [figure 5(c)] with the applied field close to zero experiences the self-field as dominant component of the local magnetic field. Then, the self-field in the thin film approximation has only B_z component, which is completely perpendicular to the surface and the current density. Therefore, only $J_{c\perp}$ is relevant and the maximum \mathbf{J} in the sample is decreased back to that value.

The last two cases, $\theta = 60^\circ$ and 80° , present similar behavior. The penetration of J_x to the sample is even smaller during the increase of the applied field [figures 6(a), 7(a)], because of the higher angles $\theta = 60^\circ, 80^\circ$. The maximum J_x component at the peak of the applied field [figures 6(b), 7(b)] is reaching 2.5 and 3 times of $J_{c\perp}$, which is the value of $J_{c\parallel}$. Again, at remanent state [figures 6(c), 7(c)] the maximum J_x component is decreased back to values around $J_{c\perp}$ because of the self-field without any parallel component of the local magnetic field.

The hysteresis loops for all angles θ of the applied field are on figure 8(a). The larger

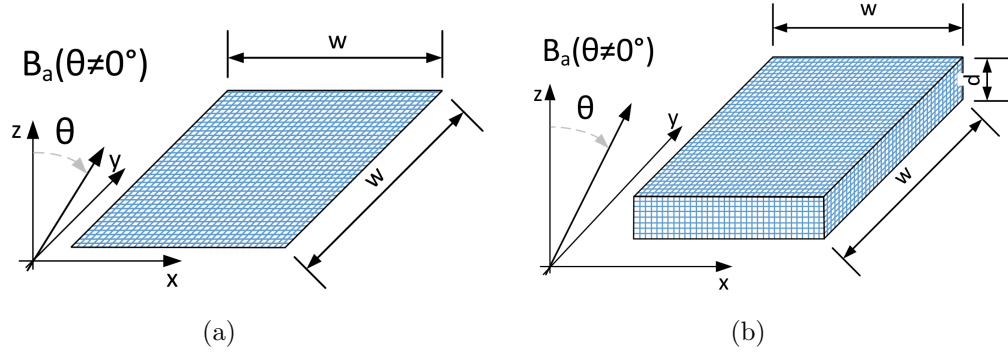


FIG. 3: Sketches of the geometry with the variable angle θ of the applied magnetic field
(a) thin strip (b) prism.

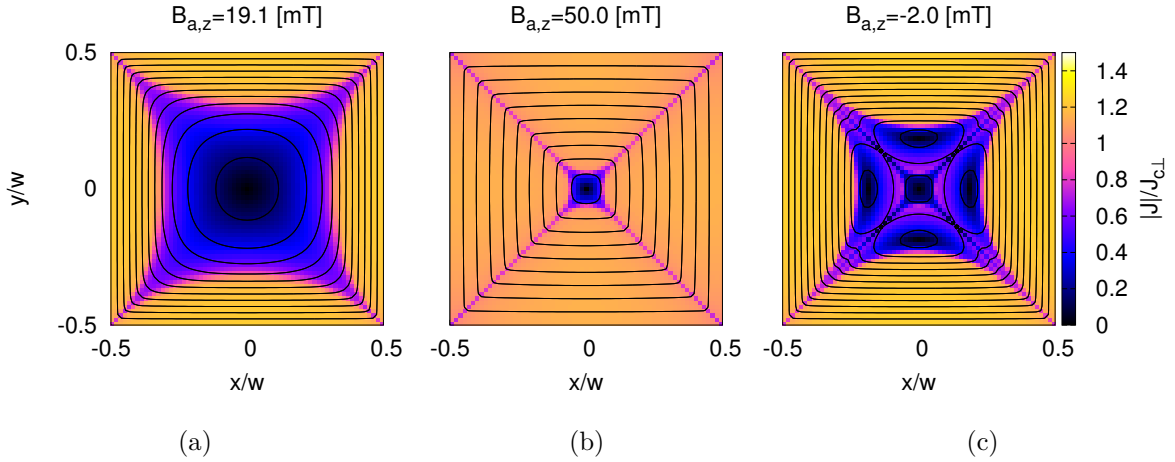


FIG. 4: Penetration process of the critical-current density in the thin film with force-free anisotropic $\mathbf{E}(\mathbf{J})$ relation. The applied magnetic field is sinusoidal with $\theta = 0$ (perpendicular to the surface), $B_{am} = 50$ mT, and $f = 50$ Hz. (a) Initial curve. (b) Peak of the applied field. (c) Quasi-remanent state. The figure also shows the current flux lines.

the applied-field angle, the higher the impact of $J_{c\parallel}$, and hence there exist places with the current density around $J_{c\parallel}$. The current density around $J_{c\parallel}$ creates higher magnetic moment in comparison to $\theta = 0^\circ$ where $|\mathbf{J}|$ is limited by $J_{c\perp}$. The self-field is dominant at the range of the applied field ± 5 mT, causing a mostly perpendicular local magnetic field, and hence $|\mathbf{J}|$ is again limited to $J_{c\perp}$. This is the reason why the magnetization is decreasing back to the same value as in the case of $\theta = 0^\circ$. We calculated the same situation with isotropic power law. The results of the isotropic case are the same for each angle θ because the perpendicular

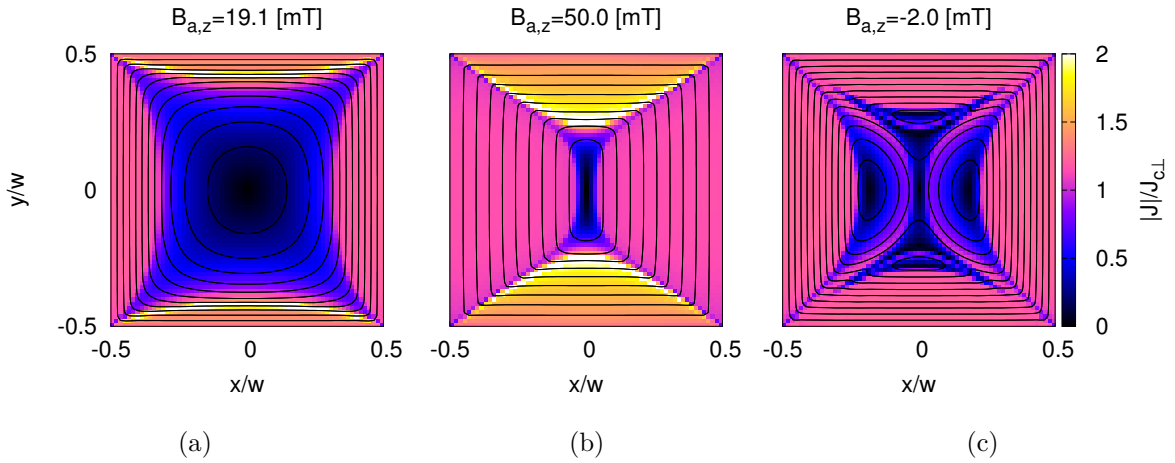


FIG. 5: The same as figure 4 but for $\theta = 45^\circ$.

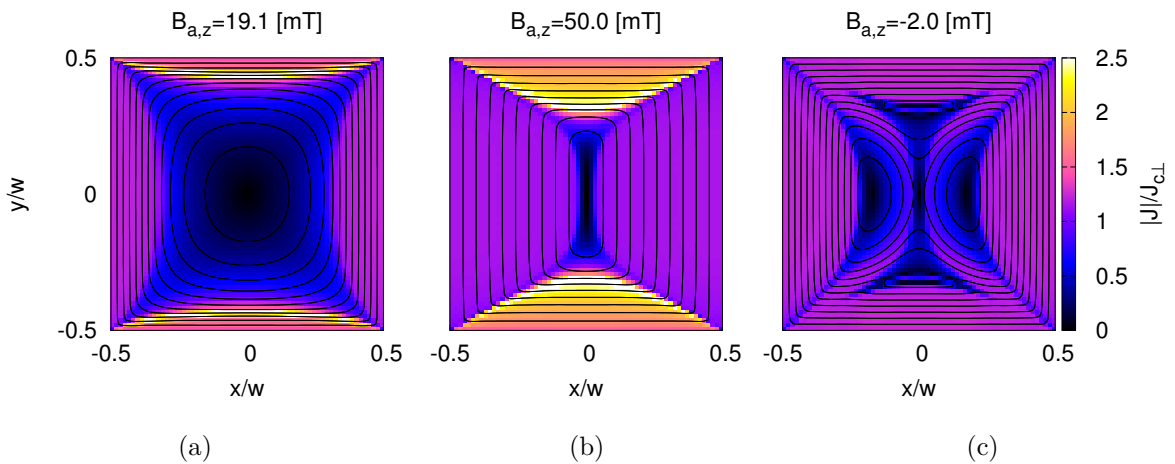


FIG. 6: The same as figure 4 but for $\theta = 60^\circ$.

applied field is the same as for $\theta = 0^\circ$ [see magnetization loops in figure 8(b)]. Consistently, these magnetization loops also agree with the anisotropic case with $\theta = 0^\circ$, since $J_c = J_{c\perp}$ for the whole loop [figure 8(a)].

2. Magnet situation

The next calculation assumes the same parameters and geometry as the previous cases. The difference is in the n -factor, with value 100, triangular waveform of the applied field of 1 mHz frequency and amplitude $B_{a,z,m} = 150$ mT. This magnetization is qualitatively similar

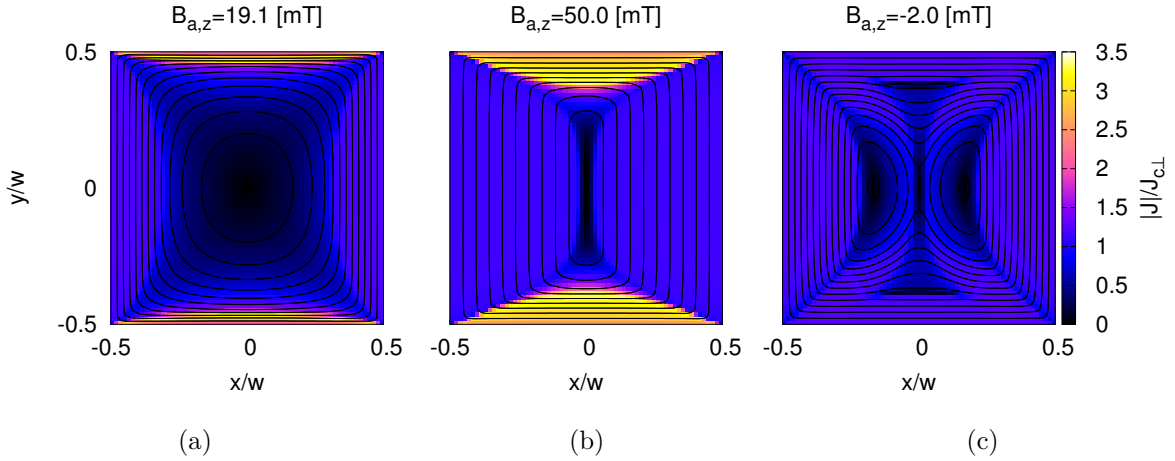


FIG. 7: The same as figure 4 but for $\theta = 80^\circ$. For sufficiently large applied fields (a,b) there appear zones with $|\mathbf{J}| \approx J_{c\perp}$ and $|\mathbf{J}| \approx J_{c\parallel}$, while at the quasi-remanent state (c) $|\mathbf{J}|$ is limited to $J_{c\perp}$.

to magnet charge and discharge. The angles of applied field are the same $\theta = 0^\circ, 45^\circ, 60^\circ, 80^\circ$. The high n -factor reduces the current density to values equal or below $J_{c\perp}$ or $J_{c\parallel}$. Another reason for reduction of current density is the very low frequency of the applied field, which allows higher flux relaxation. The constant ramp rate causes that the magnetization loops are flat after the sample is fully saturated [figure 9(b)]. The case of $\theta = 0^\circ$ induces only current density perpendicular to the applied field, and hence magnetization loop is horizontal at the remanent state. Again, we see a minimum at remanence for higher θ .

The last thin film example assumes anisotropic power law with two critical current densities, which depends on the magnetic field according Kim model $J_{c\parallel}(B)$, $J_{c\perp}(B)$. The dependence is on figure 1(b). The magnetic field \mathbf{B} is calculated in the same time step $\mathbf{B}(t)$ as the functional is minimized, and hence now the remanent state is straightforwardly for $\mathbf{B} = 0$ as it is shown on figure figure 10(b). The $B_{a,z}$ component of the maximum applied field is 300 mT and it is the same for all angles θ . The magnetization of the sample [figure 10(a)] is higher close to the remanent state, since the applied field is close to zero and the self-field only slightly decreases the critical current density. With increasing the applied field from the zero-field-cool situation, the sample becomes fully saturated already at 40 mT. With further increase of the applied field, the Kim dependence causes a decrease in $J_{c\parallel}, J_{c\perp}$ and $|\mathbf{J}|$, decreasing the magnitude of the magnetization. The highest magnetization is at

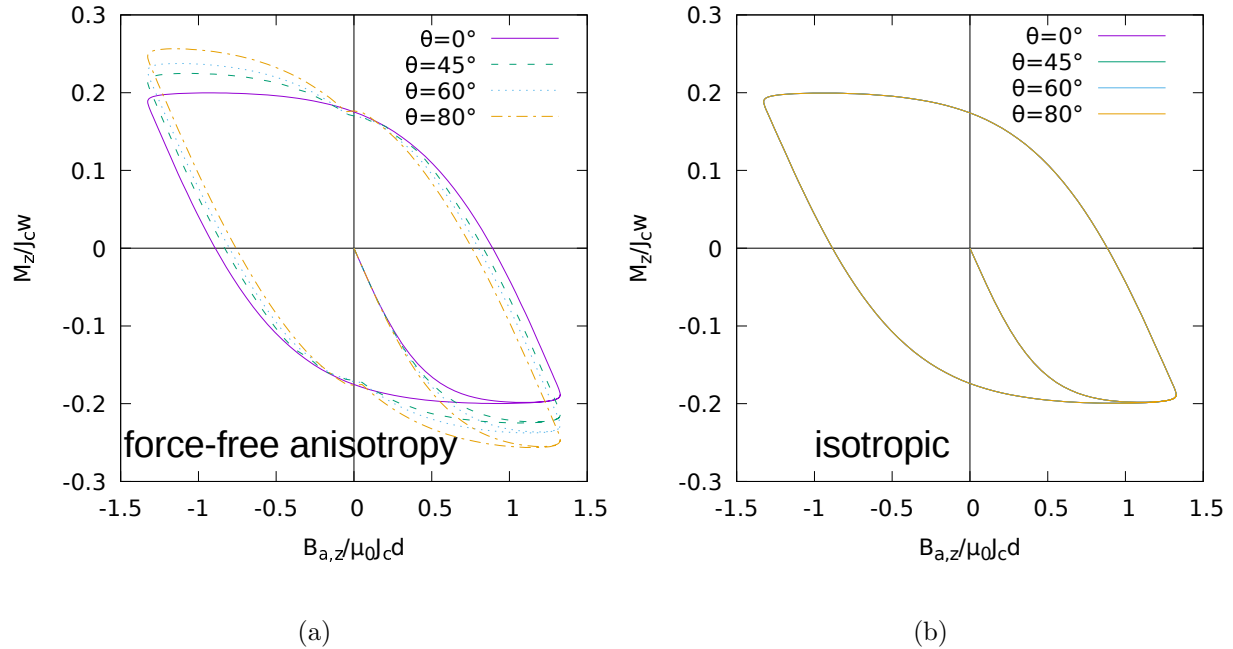


FIG. 8: Force free anisotropy increases the magnetization at the peak of the applied field. Case for thin film with n value 30, sinusoidal applied magnetic field $B_{a,z} = 50.0$ mT and $f = 50$ Hz. (a) Force-free anisotropic power law. (b) Isotropic power law.

the applied field with $\theta = 80^\circ$, in spite of $|\mathbf{B}_a|$ being the largest and hence reducing the most $J_{c\perp}$ and $J_{c\parallel}$. The cause is that there still exist areas with current density around $J_{c\parallel}$. At the remanent state, we can see again reduction of magnetization to the level of $\theta = 0^\circ$ [figure 10(b)].

B. Anisotropic force-free effects in prisms

1. Current density in prisms.

In the following, we analyze the force-free effects in a prisms. We model the prisms with the same dimensions as thin film 12×12 mm but thickness 1 mm. The mesh of the sample is created by elongated cells, which we explain in A. The total number of cells is $31 \times 31 \times 15$, which corresponds to around 43000 degrees of freedom. The frequency of the applied field is 50 Hz and the amplitude of the z component of \mathbf{B}_a is 50 mT for all angles $\theta = 0^\circ, 45^\circ, 60^\circ, 80^\circ$; and hence the total amplitude is $B_{a,m} = 50, 70.7, 100$ and 287.9

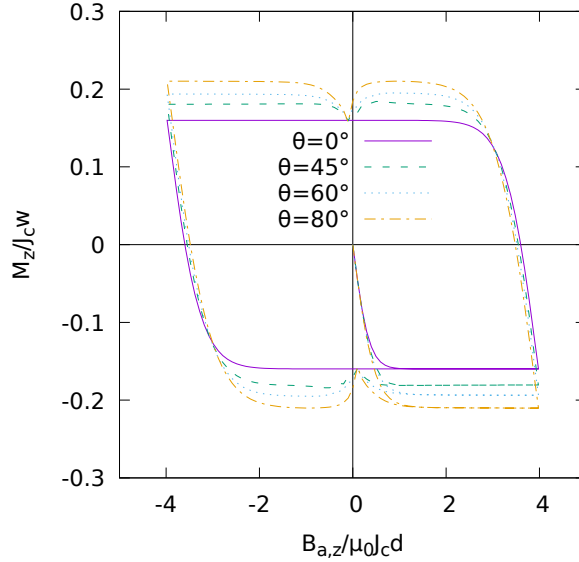


FIG. 9: For a triangular waveform of the applied field, the minimum at remanence of the hysteresis loops is very pronounced. Calculations for the force-free anisotropic power law of $n=100$ and triangular applied magnetic field with $B_{a,m} = 150.0$ mT, $B_{a,zm} = 50$ mT and $f = 1$ mHz.

mT, respectively. The critical current densities are chosen so that the sheet critical current density $K_c \equiv J_c d$ is the same as for the thin film, being d the sample thickness. Further values are $J_{c\perp} = 3 \cdot 10^7$ A/mm², $J_{c\parallel} = 3J_{c\perp}$ and $n=30$.

The force-free effects are modelled with the anisotropic power law and the sharp dependence of $J_{c\parallel}$ with the magnetic field of figure 1(a). Then, the functional is minimized with the magnetic field from the previous time step like in the case of thin film.

The first case is with applied field $\theta=0^\circ$. We calculated the average current density over thickness. The penetration of the average current density into the prism at the peak of applied field is on figure 11, where we add the case of thin film for comparison. There is a small difference in penetration depth of the current density, which can be explained by different number of elements in the x and y directions. The result of prism looks coarser, but we solved 10 times higher number of degrees of freedom compared to the thin film, since the prism is a 3D object. The smaller penetration in thin film is more visible in the profiles over the x and y directions on the sample center [figure 11(c),(d)], also for a lower applied field. For these planes, J_z vanishes due to symmetry, although $J_z \neq 0$ at other regions [50].

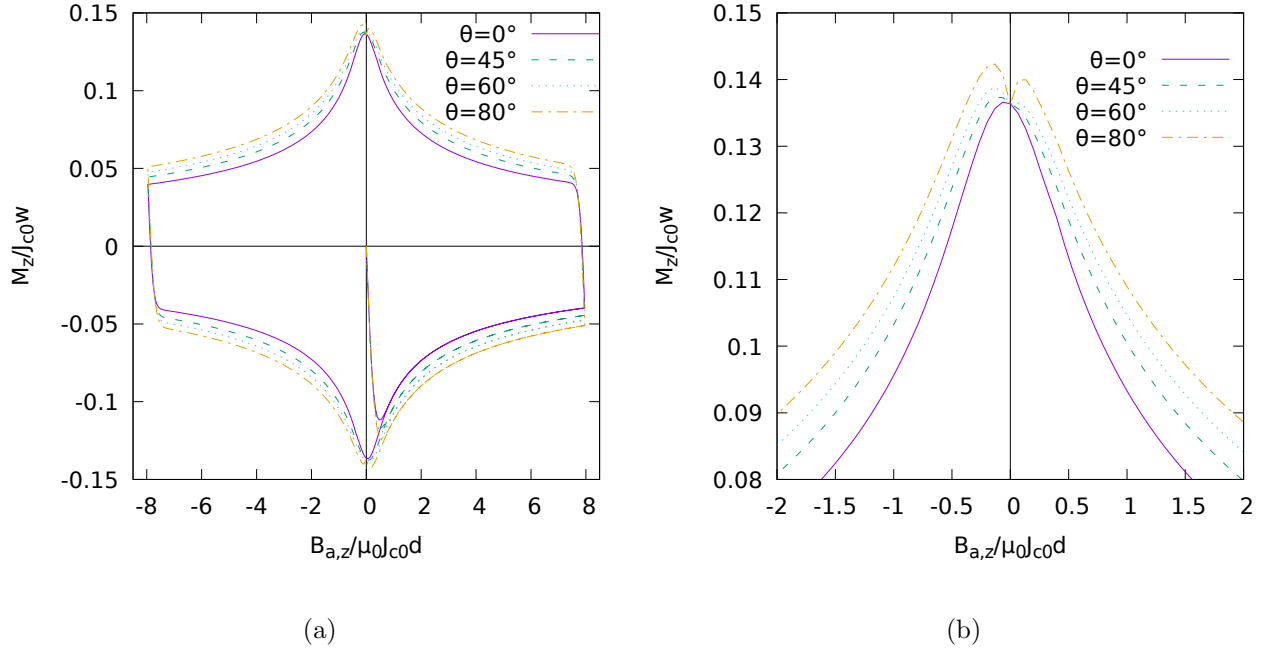


FIG. 10: (a) With a Kim-like dependence of $J_{c\parallel}$ and $J_{c\perp}$, the area of the magnetization loop increases with θ due to force-free effects. (b) This zoom at low applied field shows the minimum of the remanence. The parameters are $n = 100$ and triangular applied magnetic field with $B_{az,m} = 300$ mT and $f = 1$ mHz.

The second case of prism is $\theta = 45^\circ$. The penetration depth of the average current density in the prism [figure 12(b)] agrees with the thin film case [figure 12(a)]. The agreement is as well in the lines of $x = 0$ and $y = 0$ [figure 12(c),(d)]. The J_y component of the current density is around $J_{c\perp}$ [figure 12(d)], but J_x is 2 times higher. The reason of the higher magnitude of J_x is that the applied field has a component in the x direction, causing force-free effects. This also causes that J_x at the penetration front reaches $J_{c\parallel}$ in the thin film, since B_z there vanishes (figure 12). The penetration depth in the prism is smaller, because of the thicker cells.

The last two cases with $\theta = 60^\circ, 80^\circ$ are similar to the appropriate cases of thin film, although with certain differences. For the angle $\theta = 60^\circ$ there is lower penetration depth from the right and left sides [figure 13(b)] than the thin film [figure 13(a)]. The angle $\theta = 80^\circ$ has even lower penetration depth from these sides [figure 14(b)] compared to thin film [figure 14(a)]. The current profiles along the x and y directions show the same behaviour of lower current penetration [figure 13(c),(d), 14(c),(d)]. The cause of lower penetration depth along

both x and y directions is due to the prism finite thickness. Since $\theta \neq 0^\circ$, there is a significant J_z component of the current density, which is around $J_{c\perp}$ [figure 16(c) $\theta = 80^\circ$].

Finally, we compare the 3D current paths in the prism at the peak of the applied field for the anisotropic case and two applied field angles $\theta = 0^\circ$ and 80° . For the first angle, the sample is fully saturated as seeing the mid planes perpendicular to the x and y axis [figure 15(a),(b)] and hence J_z almost vanishes [figure 15(c)]. For the second angle ($\theta = 80^\circ$), the J_y component of the current density is also saturated in most of the volume [figure 16(b)]. Now, the border between positive and negative J_y component follows roughly the direction of the applied magnetic field. The J_x component is not saturated in the sample [figure 16(a)] and the highest penetration depth is at the centre of the prism. Since the current loops are almost perpendicular to the angle of the applied field, there exists a substantial J_z component [figure 16(c)].

2. Magnetization loops in prisms.

We calculated the hysteresis loops for all previous cases (figure 17). In order to explain all effects, we also analyzed the same situation with isotropic power law (figure 18). The M_z component of the magnetization is lower for higher applied magnetic field angle θ [figure 18(b)]. This is because the path of the screening current loops tilts away from the xy plane. The M_x component is zero for $\theta = 0^\circ$ [figure 18(a)], since the current path is only in the xy plane. This also causes an increase of the M_x component with increasing θ . This geometry effect can be reduced by decreasing the prism thickness. Consistently, M_x vanishes at $\theta = 0$ because the current loops are mainly in the xy plane and the remaining bending in the z direction is symmetric (see figure 5 of [50]).

The hysteresis loops with anisotropic $\mathbf{E}(\mathbf{J})$ relation have more effects. On one hand, increasing the angle θ enlarges the region with $|\mathbf{J}| \approx J_{c\parallel}$, increasing also M_z . On the other hand, by increasing θ , the tilt increases, reducing M_z . The result is an increase in M_z with θ but for $\theta = 80^\circ$ this increase is smaller than for the thin film [figure 17(b)]. The magnetization in the x direction [figure 17(a)] shows mostly the same behavior as isotropic case. The difference is only in a peak of the magnetization around the zero applied field. This peak of the magnetization appears for both components, M_x and M_z . The reason of this peak is the following. For very small magnetic fields, the self-field dominates. Close

to the top (highest z) and bottom (lowest z) of the sample, the self-field is parallel to the surface. Then, part of the sample experiences a local magnetic field parallel to the current density, increasing J_c towards $J_{c\parallel}$. For applied fields much larger than the self-field, the magnetic field follows the direction of the applied field. This applied field is not perfectly parallel to the surface, causing a lower J_c .

Another calculation with isotropic $\mathbf{E}(\mathbf{J})$ relation shows the geometry effects due to different thickness of the prism ($d = 1, 0.6, 0.5, 0.1$) while keeping a constant sheet current density. First we check that for only perpendicular applied field, the prism results approach to the thin film by reducing the thickness. Figure 19 shows that the normalized z component $M_z/J_c w$ is roughly the same for all thicknesses d . This figure also tells us that the magnetic moment m_z almost does not depend on d , since $M_z/J_c w = m_z/J_c d w^3$ and we keep both $J_c d$ and w constant. For a magnetic field angle θ of 80° , M_z increases with decreasing the sample thickness, since the screening current is forced to flow closer to the xy plane [figure 20(b)]. However, the other normalized component, $M_x/J_c d$, increases with the thickness d , due to the increase of the area of the projection of the current loops in the yz plane.

IV. CONCLUSIONS

This article systematically studied the anisotropic force-free effects in superconducting thin films and prisms under uniform applied magnetic field making on angle θ with the surface. In order to better understand all effects, we performed modelling with isotropic and anisotropic $\mathbf{E}(\mathbf{J})$ relation due to force-free effects.

For this purpose, we use the MEMEP 3D numerical method [48]. We further developed the model in order to enable elongated cells, to reduce the total number of elements or enable to model relatively long or thin structures without further increasing the total number of elements. In particular, we studied the elliptical double critical state model with a continuous $\mathbf{E}(\mathbf{J})$ relation[54].

In the thin film force-free model, we calculated the gradual penetration of the current density. We found at the remanent state that J decreases to $J_{c\perp}$ and the magnetization increases with the angle θ . The magnetization of the isotropic film is the same for all applied field angles, when comparing for the same perpendicular component of the applied magnetic field and its amplitude. The anisotropic model, both with and without $J_c(B)$ dependence,

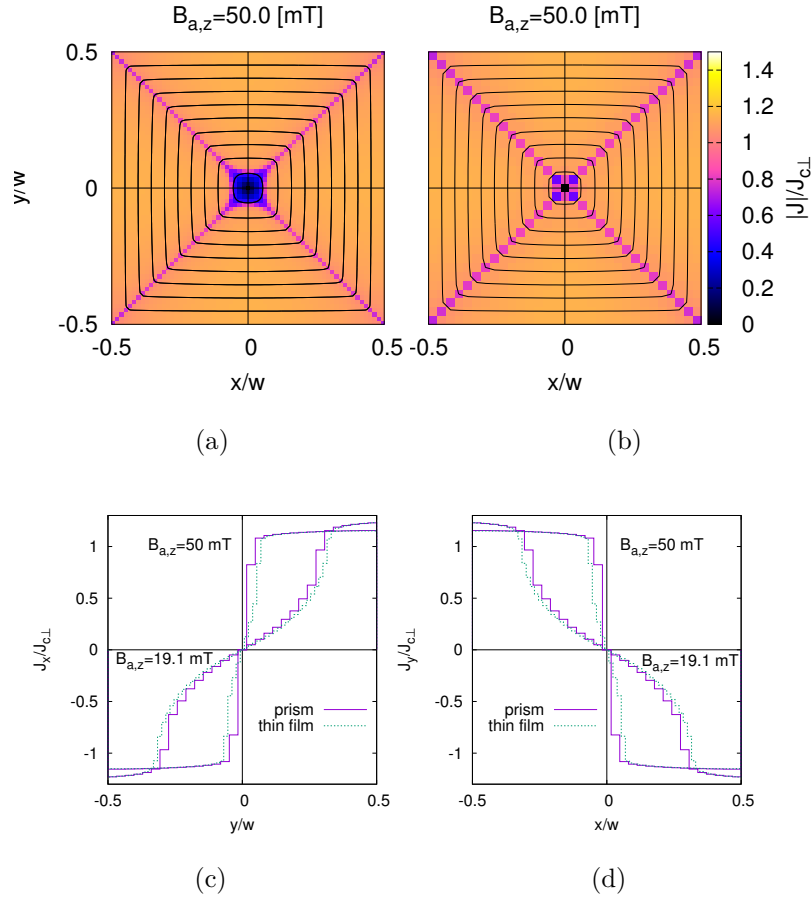


FIG. 11: For low angles of the applied field, the thickness-averaged current density in a prism agrees with the thin film. Thickness-average current density and flux lines for a thin film (a) and prism (b). Plots (c) and (d) show the current density at the $x = 0$ and $y = 0$ lines, respectively. The parameters are $\theta = 0$, $B_{a,z,m} = 50$ mT and $f = 50$ Hz.

shows a minimum of the magnetization at the remanent state for $\theta \neq 0$. The cause is the absence of any parallel component of the local magnetic field to the current density, avoiding J_c enhancement due to force-free effects. In superconducting prisms, we observed 3D current paths. The average current density over thickness shows good agreement with thin film sample. However, for high applied magnetic field angles there appear small differences. The M_x component is increasing with the angle θ , because of the significant increase of J_z . The M_z slightly decreases due to the tilt in the screening currents. The magnetization loops show a peak after the remanent state due to the influence of the parallel component of the self-field, increasing J_c up to $J_{||}$ at part of the sample. This effect is not present for the thin

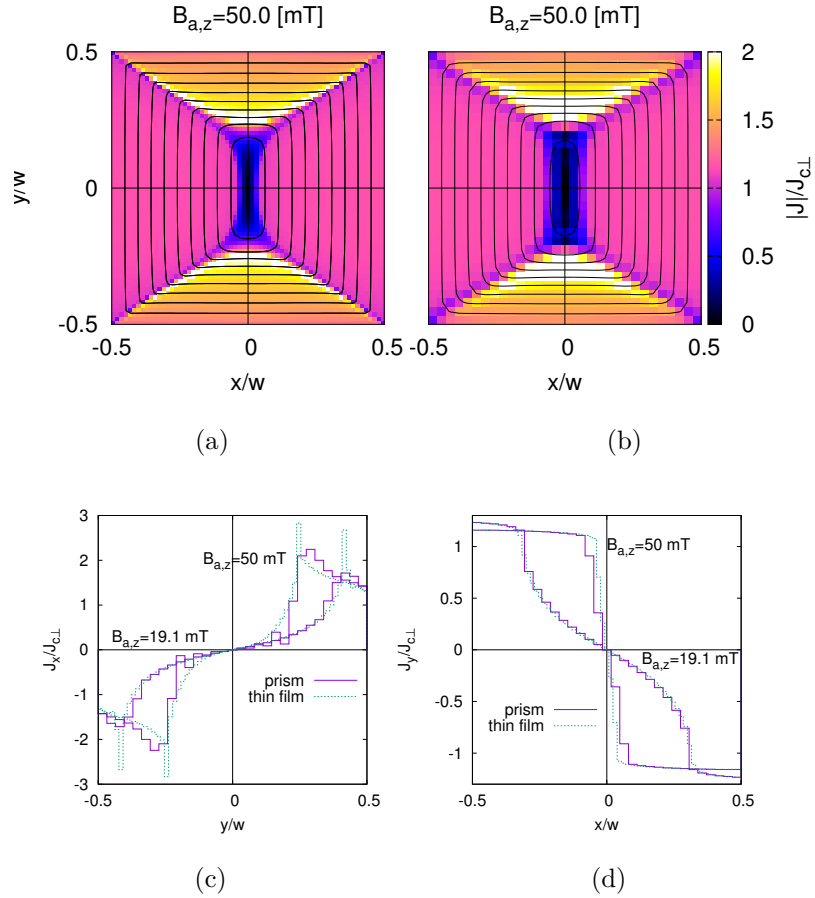


FIG. 12: The same as figure 11 but for $\theta = 45^\circ$. The transverse component of the applied field amplitude of $B_{a,z,m} = 50$ mT requires a total amplitude of $B_{am} = 70.7$ mT.

film approximation because the parallel component of the self-field is neglected. Calculations for several prism thicknesses down to $100 \mu\text{m}$ support the validity of the results.

We expect that the thin film geometry may not be a good approximation for study force-free effects in magnetization measurements. This study confirmed that the MEMEP 3D method is suitable for any $\mathbf{E}(\mathbf{J})$ relation and it can be solved with a relatively high number of degrees of freedom and relatively thin samples in 3D space. Further work could be to investigate different shapes of the sample and speed up the calculation, maybe by multi-pole expansion.

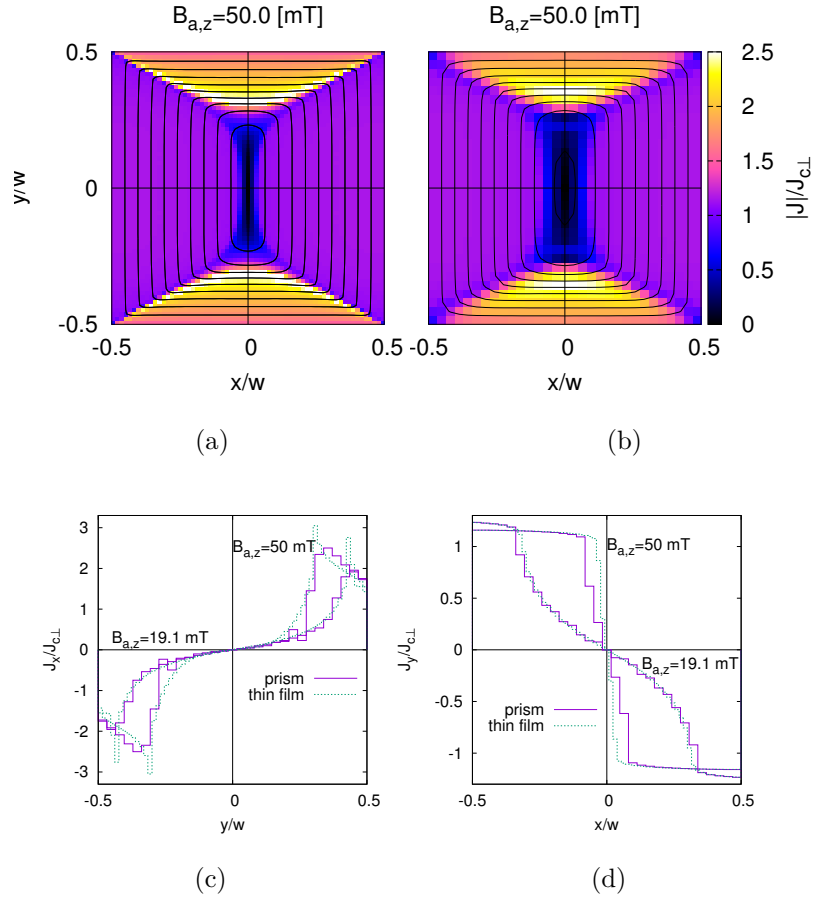


FIG. 13: The same as figure 11 but for $\theta = 60^\circ$ ($B_{a,z,m} = 50$ mT and $B_{am} = 100$ mT). A slightly lower critical-current penetration can be observed from the prism (b,d) compared to the film (a,c).

ACKNOWLEDGEMENTS

Authors acknowledge the use of computing resources provided by the project SIVVP, ITMS 26230120002 supported by the Research & Development Operational Programme funded by the ERDF, the financial support of the Grant Agency of the Ministry of Education of the Slovak Republic and the Slovak Academy of Sciences (VEGA) under contract No. 2/0097/18, and the support by the Slovak Research and Development Agency under the contract No. APVV-14-0438.

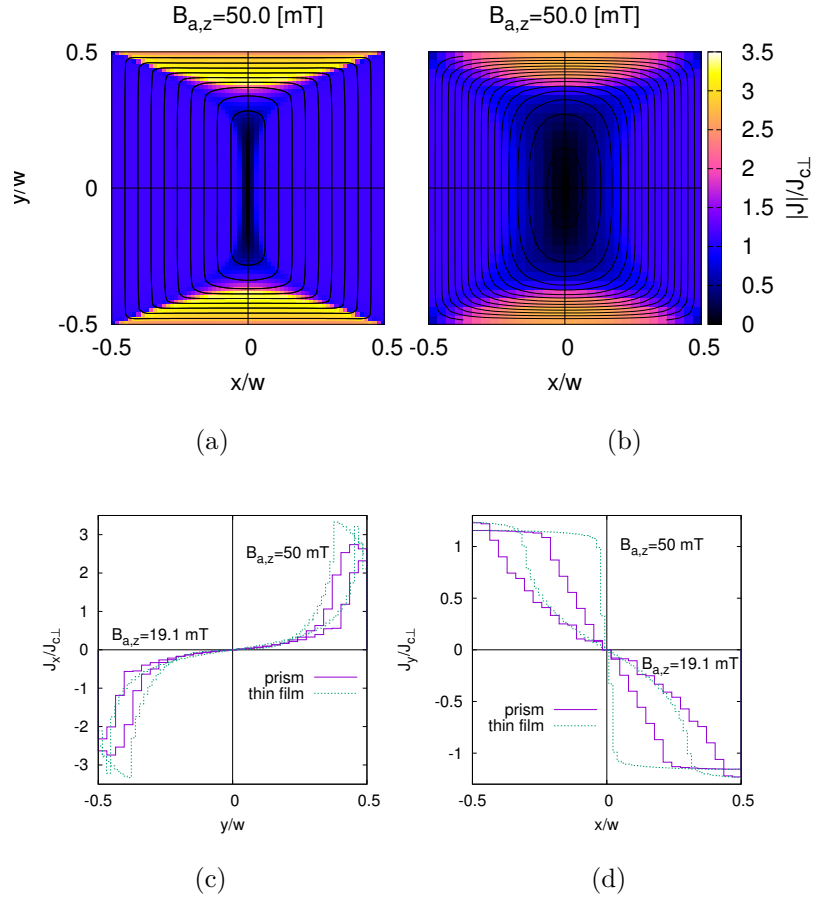


FIG. 14: The same as figure 11 but for $\theta = 80^\circ$ ($B_{az,m} = 50$ mT and $B_{am} = 287.9$ mT). The prism (b,d) presents a substantially lower penetration of the critical-current density than the film (a,c).

Appendix A: Elongated cells

The elongated cells are cells with different geometry ratio than square (for 2D) or cubic (for 3D). These cells allow to model geometries such as long thin film, or thin/thick bulk. The elongated cells enable to reduce the total number of elements, and hence reduce the computing time. A key issue is the calculation of the interaction matrix between elemental surfaces (or “surfaces”). The interaction matrix between surfaces i and j of type $s \in \{x, y, z\}$ is generally [48]

$$a_{sij} = \frac{\mu_0}{4\pi V_{si} V_{sj}} \int_{V_{si}} d^3 \mathbf{r} \int_{V_{sj}} d^3 \mathbf{r}' \frac{h_{si}(\mathbf{r}) h_{sj}(\mathbf{r}')}{|\mathbf{r} - \mathbf{r}'|}, \quad (\text{A1})$$

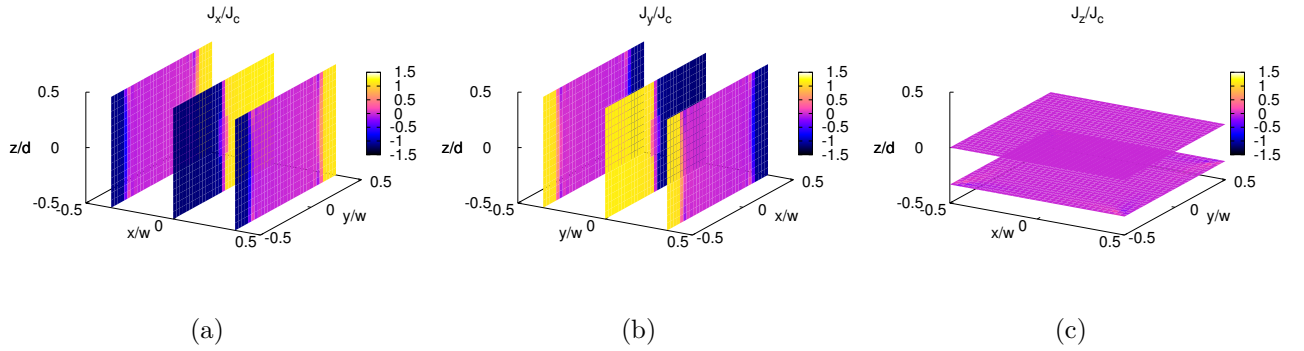


FIG. 15: Current density in a prism with force-free anisotropy at the peak of the applied field and $w = 12$ mm, $d = 1$ mm, $\theta = 0^\circ$, and $B_{az,m} = 50$ mT. The current density components are: (a) J_x (b) J_y (c) J_z . Note that the plotted planes in (b) are not the same as (a,c).

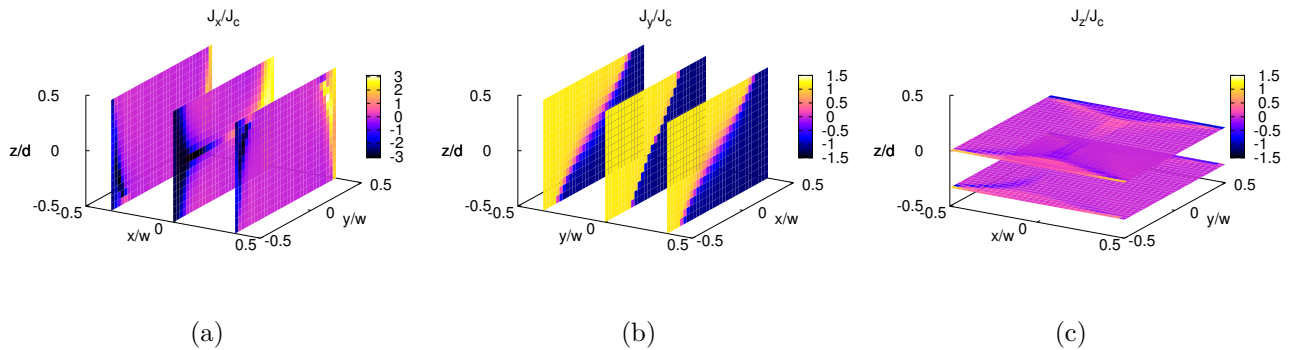


FIG. 16: The same as figure 15 but for $\theta = 80^\circ$ ($B_{am} = 287.9$ mT).

with

$$V_{si} \equiv \int_V d^3\mathbf{r} h_{si}(\mathbf{r}). \quad (\text{A2})$$

The first-order interpolation functions $h_{si}(\mathbf{r})$ are defined as in figure 21(b) for coordinate $r_s = r_x$, vanishing outside the two neighboring cells in the r_s direction.

In the case of square or cubic cells or square sub-elements, the self-interaction term a_{sii} can be calculated by the approximated analytical formula

$$a_{sii} \approx \frac{\mu_0}{4\pi V_{si}^2} \int_{V_{si}} d^3\mathbf{r} \int_{V_{si}} d^3\mathbf{r}' \frac{1}{|\mathbf{r} - \mathbf{r}'|}. \quad (\text{A3})$$

The integral $\int_{V_{si}} d^3\mathbf{r} \int_{V_{sj}} d^3\mathbf{r}' (1/|\mathbf{r} - \mathbf{r}'|)$ on a rectangular prism is a lengthy analytical formula.

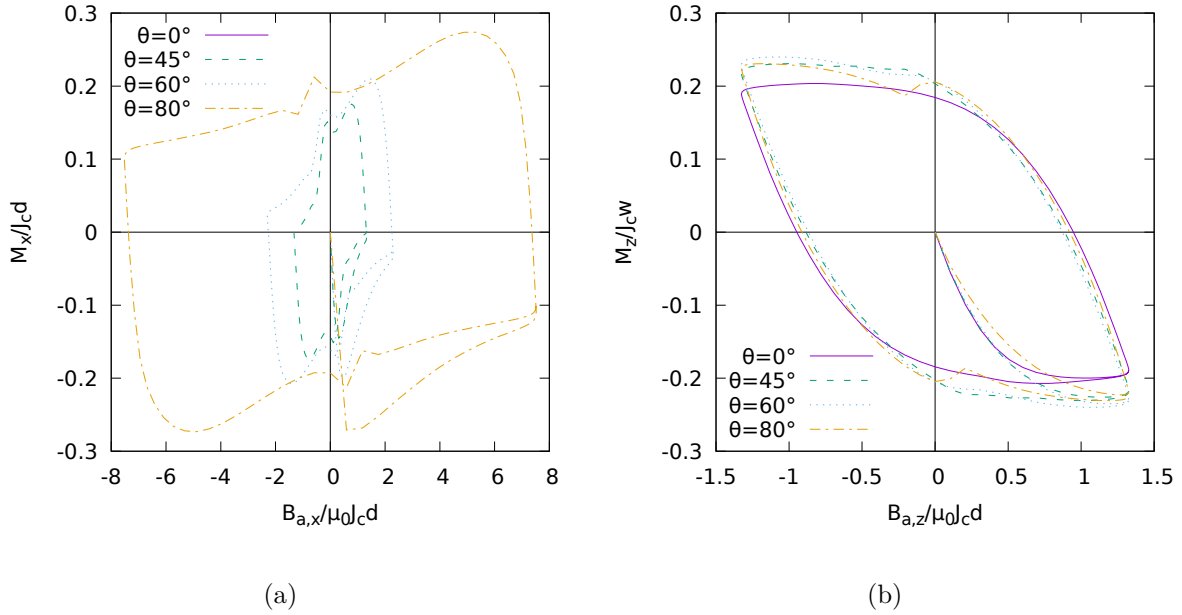


FIG. 17: The influence of the applied field angle to the magnetization loops in a prism is somewhat different than that of a thin film with the same sheet critical current density $J_c d$. Case of anisotropic $\mathbf{E}(\mathbf{J})$ relation and constant $J_{c\parallel}$, $J_{c\perp}$, $n = 30$, sinusoidal applied magnetic field with $B_{a,z} = 50.0$ mT and $f = 50$ Hz. (a) The x component of the magnetization M_x component. (b) M_z .

For a cube and a square surface, the expression can be greatly simplified as

$$a_{sii} \approx \frac{\mu_0}{4\pi L_{si}} \left\{ \frac{1 + \sqrt{2} - 2\sqrt{3}}{5} - \frac{\pi}{3} + \ln \left[\left(1 + \sqrt{2}\right) \left(2 + \sqrt{3}\right) \right] \right\} \quad (\text{A4})$$

for a cube of side L_{si} [55] and

$$a_{sii} \approx \frac{\mu_0}{\pi L_{si}} \left\{ \frac{1 - \sqrt{2}}{3} + \ln \left(1 + \sqrt{2}\right) \right\} \quad (\text{A5})$$

for a thin prism [56] with thickness d much smaller than its side L_{si} . For equation (A3) we assumed that the current density is uniform in the volume of influence, defined as the volume between surface i of type s and the centre of the neighbouring cells in the s direction (see figure 21(a) for $s = x$). The average vector potential a_{sij} is calculated by approximation everywhere else, $i \neq j$

$$a_{sij} \approx \frac{\mu_0}{4\pi |r_{si} - r_{sj}|}, \quad (\text{A6})$$

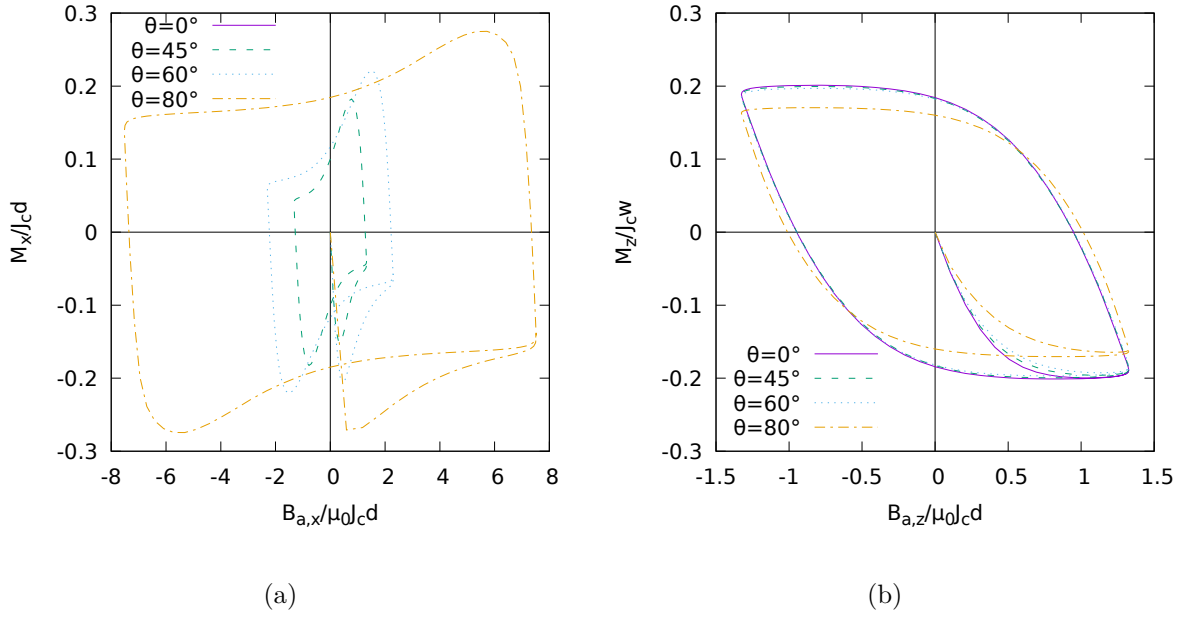


FIG. 18: The same as figure 17 but for isotropic $\mathbf{E}(\mathbf{J})$. Several differences appear from the anisotropic case, such as the peaks close to the remanence in figure 17.

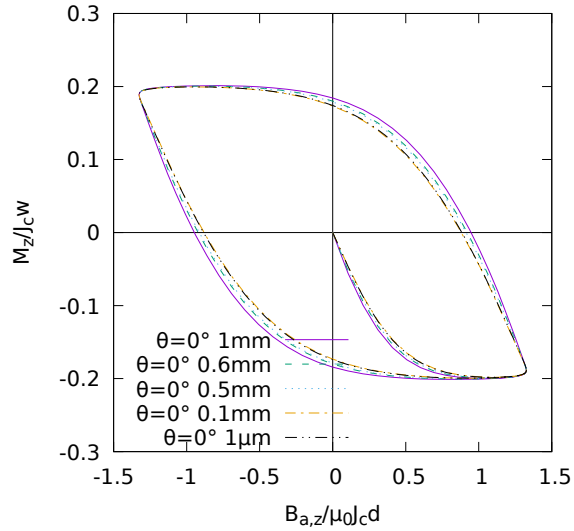


FIG. 19: For isotropic $\mathbf{E}(\mathbf{J})$ in prisms and $\theta = 0$, the normalized magnetization converges to the thin film situation. The properties are $n = 30$, sinusoidal applied magnetic field

$$B_{a,z} = 50.0 \text{ mT and } f = 50 \text{ Hz.}$$

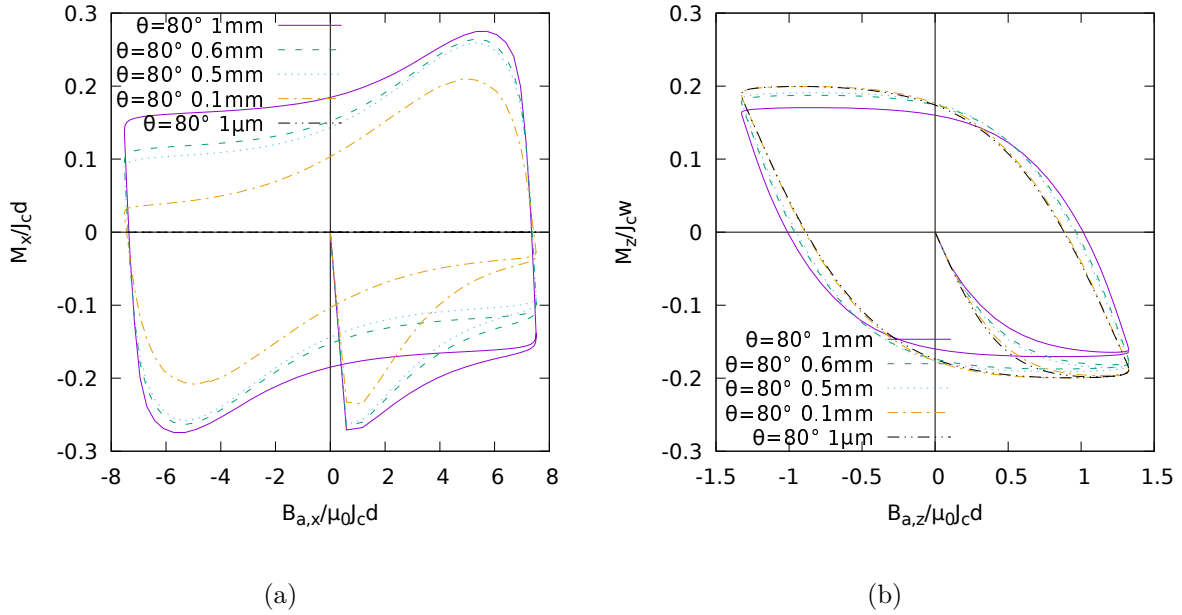


FIG. 20: Hysteresis loops of prisms with several thicknesses d and the same width w with isotropic $\mathbf{E}(\mathbf{J})$ relation and constant J_c , $n=30$, and sinusoidal applied magnetic field with $B_{a,z}=50.0$ mT and $f=50$ Hz. (a) M_x component. (b) M_z component

where r_{si} is the centre of surface i of type s .

In the case of elongated cells, the interaction matrix of the vector potential, a_{sij} needs to be calculated numerically. The numerical calculation splits the surrounded area of two surfaces into small square sub-elements (figure 21(a)). The average vector potential of the two surfaces is integrated over all sub-elements, which contain surfaces again. The sub-elements are calculated in the same way as square cells, but sub-elements are multiplied by the linear interpolations functions $h_{si}(\mathbf{r})$, $h_{sj}(\mathbf{r})$ at the centre of the sub-element surfaces with indexes l, m , being \mathbf{r}_{sl} and \mathbf{r}_{sm} . Elongated cells contain as many sub-elements in order to reach as square as possible shape. In general, the average vector potential generated by sub-element l on sub-element m is

$$a_{sijlm} = \frac{\mu_0}{4\pi V_{sl} V_{sm}} \int_{V_{sl}} d^3\mathbf{r} \int_{V_{sm}} d^3\mathbf{r}' \frac{h_{si}(\mathbf{r}_{sl}) h_{sj}(\mathbf{r}_{sm})}{|\mathbf{r} - \mathbf{r}'|}, \quad (\text{A7})$$

where V_{sl} and V_{sm} are the volume of influence of the sub-elements, as defined in figure 21(a). For $l \neq m$, we approximate the integral above by

$$a_{sijlm} \approx \frac{\mu_0 h_{si}(\mathbf{r}_{sl}) h_{sj}(\mathbf{r}_{sm})}{4\pi |\mathbf{r}_{sl} - \mathbf{r}_{sm}|}, \quad (\text{A8})$$

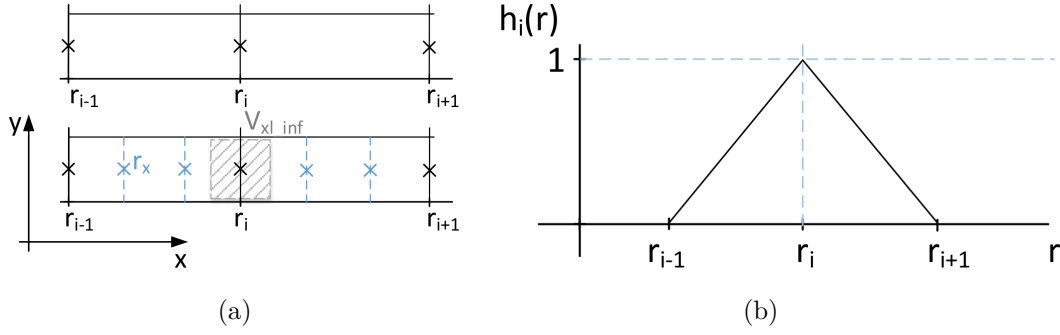


FIG. 21: (a) Dividing elongated cells into sub-elements enables to compute accurate interaction matrix elements. Solid lines: original elongated mesh. Dash lines: sub-elements mesh. (b) Interpolation $h_i(r)$ function.

where V_{sl} is the volume of the influence of the sub-elements, defined in figure 21(a). When l corresponds to the sub-element m both in position and size, we use the approximated formula for uniform current density in the sub-element

$$a_{sijll} \approx \frac{\mu_0 h_{si}(\mathbf{r}_{sl}) h_{sj}(\mathbf{r}_{sl})}{4\pi V_{sl}^2} \int_{V_{sl}} d^3\mathbf{r} \int_{V_{sl}} d^3\mathbf{r}' \frac{1}{|\mathbf{r} - \mathbf{r}'|}. \quad (\text{A9})$$

Following the same steps as for equation (A3), a_{sijll} becomes

$$a_{sijll} \approx \frac{\mu_0 h_{si}(\mathbf{r}_{sl}) h_{sj}(\mathbf{r}_{sl})}{4\pi L_{sl}} \cdot \left\{ \frac{1 + \sqrt{2} - 2\sqrt{3}}{5} - \frac{\pi}{3} + \ln \left[(1 + \sqrt{2}) (2 + \sqrt{3}) \right] \right\} \quad (\text{A10})$$

for a cube of side L_{sl} and

$$a_{sijll} \approx \frac{\mu_0 h_{si}(\mathbf{r}_{sl}) h_{sj}(\mathbf{r}_{sl})}{\pi L_{sl}} \left\{ \frac{1 - \sqrt{2}}{3} + \ln (1 + \sqrt{2}) \right\} \quad (\text{A11})$$

for a thin prism of side L_{sl} .

-
- [1] D. C. Larbalestier, J.Jiang, U. P. Trociewitz, F. Kametami, C. Scheuerlein, M. Dalban-Canassy, M. Matras, P. Chen, N. C. craig, P. J. Lee, and E. E. Hellstrom, “Isotropic round-wire multifilament cuprate superconductor for generation of magnetic fields above 30 T,” *Nature Materials* **13**, 375–381 (2014).

- [2] K. Kim, K. R. Bhattarai, J. Y. Jang, Y. J. Hwang, K. Kim, S. Yoon, S. Lee, and S. Hahn, “Design and performance estimation of a 35 T 40 mm no-insulation all-REBCO user magnet,” *Supercond. Sci. Technol.* **30** (2017).
- [3] D. Park, J. Bascunan, P. Michael, J. Lee, S. Hahn, and Y. Iwasa, “Construction and test results of coils 2 and 3 of a 3-nested-coil 800-MHz REBCO insert for the MIT 1.3-GHz LTS/HTS NMR Magnet,” *IEEE Trans. Appl. Supercond.* **28** (2018).
- [4] J. Liu and Y. Li, “High-Field Insert With Bi- and Y-Based Tapes for 25-T All-Superconducting Magnet,” *IEEE Trans. Appl. Supercond.* **26** (2016).
- [5] P. J. Masson, M. Breschi, T. Pascal, and C. Luongo, “Design of HTS axial flux motor for aircraft propulsion,” *IEEE Trans. Appl. Supercond.* **17** (2007).
- [6] P. J. Masson, K. Ratelle, P. A. Delobel, A. Lipardi, and C. Lorin, “Development of a 3D sizing model for all-superconducting machines for turbo-electric aircraft propulsion,” *IEEE Trans. Appl. Supercond.* **23**, 3600805 (2013).
- [7] T. Yanamoto, M. Izumi, K. Umemoto, T. Oryu, Y. Murase, and M. Kawamura, “Load test of 3-MW HTS motor for ship propulsion,” *IEEE Trans. Appl. Supercond.* **27** (2017).
- [8] B. Gamble, G. Snitchler, and T. MacDonald, “Full power test of a 36.5 MW HTS propulsion motor,” *IEEE Trans. Appl. Supercond.* **21**, 1083–1088 (2011).
- [9] JS. Jeong, DK. An, JP. Hong, HJ. Kim, and YS. Jo, “Design of a 10-MW-Class HTS homopolar generator for wind turbines,” *IEEE Trans. Appl. Supercond.* **27** (2017).
- [10] A.B. Abrahamsen, N. Mijatovic, E. Seiler, T. Zirngibl, C. Træholt, P.B. Nørgård, N.F. Pedersen, N.H. Andersen, and J. Østergaard, “Superconducting wind turbine generators,” *Supercond. Sci. Technol.* **23**, 034019 (2010).
- [11] SUPRAPOWER-EU project. Superconducting light generator for large offshore wind turbines. <http://www.suprapower-fp7.eu/>.
- [12] E. Volkov, V. Vysotsky, and V. Firsov, “First russian long length HTS power cable,” *Physica C-Superc. and its apl.* **482**, 87–91 (2012).
- [13] M. Yagi, J. Liu, S. Mukoyama, T. Mitsuhashi, J. Teng, N. Hayakawa, W. Wang, A. Ishiyama, N. Amemiya, T. Hasegawa, T. Saitoh, O. Maruyama, and T. Ohkuma, “Experimental results of 275-kV 3-kA REBCO HTS power cable,” *IEEE Trans. Appl. Supercond.* **25** (2015).
- [14] S. Hellmann, M. Abplanalp, L. Hofstetter, and M. Noe, “Manufacturing of a 1-MVA-Class superconducting fault current limiting transformer with recovery-under-load capabilities,” *IEEE*

- Trans. Appl. Supercond. **27** (2017).
- [15] N. Glasson, M. Staines, N. Allpress, M. Pannu, J. Tanchon, E. Pardo, R. Badcock, and R. Buckley, “Test results and conclusions from a 1 MVA superconducting transformer featuring 2G HTS roebel cable,” *IEEE Trans. Appl. Supercond.* **27** (2017).
- [16] S. Schwenterly, B. McConnell, J. Demko, A. Fadnek, J. Hsu, F. List, M. Walker, D. Hazelton, F. Murray, J. Rice, C. Trautwein, X. Shi, R. Farrell, J. Bascunan, R. Hintz, S. Mehta, N. Aversa, J. Ebert, B. Bednar, D. Neder, A. McIlheran, P. Michel, J. Nemeč, E. Pleva, A. Swenton, N. Swets, R. Longsworth, RC. Longsworth, R. Johnson, R. Jones, J. Nelson, R. Degeneff, and S. Salon, “Performance of a 1-MVA HTS demonstration transformer,” *IEEE Trans. Appl. Supercond.* **9**, 680–684 (1999).
- [17] S. Mehta, “US effort on HTS power transformers,” *Physica C* **471**, 1364–1366 (2011).
- [18] T. Pascal, A. Badel, G. Auran, and GS. Pereira, “Superconducting fault current limiter for ship grid simulation and demonstration,” *IEEE Trans. Appl. Supercond.* **27** (2017).
- [19] Y. Xin, W. Gong, Y. Sun, J. Cui, H. Hong, X. Niu, H. Wang, L. Wang, Q. Li, J. Zhang, Z. Wei, L. Liu, H. Yang, and X. Zhu, “Factory and field tests of a 220 kV/300 MVA statured iron-core superconducting fault current limiter,” *IEEE Trans. Appl. Supercond.* **23** (2013).
- [20] A. Morandi, “State of the art of superconducting fault current limiters and their application to the electric power system,” *Physica C* **484**, 242–247 (2013).
- [21] J. Šouc, F. Gömöry, and M. Vojenčiak, “Coated conductor arrangement for reduced AC losses in a resistive-type superconducting fault current limiter,” *Supercond. Sci. Technol.* **25**, 014005 (2012).
- [22] J. Kozak, M. Majka, T. Blazejczyk, and P. Berowski, “Tests of the 15-kV class coreless superconducting fault current limiter,” *Supercond. Sci. Technol.* **26** (2016).
- [23] J.H. Durrell, S.H. Mennema, C. Jooss, G. Gibson, Z. H. Barber, H.W. Zandbergen, and J.E. Evetts, “Flux line lattice structure and behavior in antiphase boundary free vicinal $\text{YBa}_2\text{Cu}_3\text{O}_{7-\delta}$ thin films,” *J. Appl. Phys.* **93**, 9869–9874 (2003).
- [24] M. Lao, J. Hecher, M. Sieger, P. Pahlke, M. Bauer R. Huhne, and M. Eisterer, “Planar current anisotropy and field dependence of J_c in coated conductors assessed by scanning hall probe microscopy,” *Supercond. Sci. Technol.* **30**, 9 (2017).
- [25] G. Blatter, M. V. Feigelman, V. B. Geshkenbein, A. I. Larkin, and V. M. Vinokur, “Vortices in high-temperature superconductors,” *Rev. Mod. Phys.* **66**, 1125 (1994).

- [26] V. Vlasko-Vlasov, A. Koshelev, A. Glatz, C. Phillips, U. Welp, and K. Kwok, “Flux cutting in high- T_c superconductors,” *Phys. Rev. B* (2015).
- [27] J.R. Clem, “Flux-line-cutting losses in type-II superconductors,” *Phys. Rev. B* **26**, 2463 (1982).
- [28] J.R. Clem, M. Weigand, J. H. Durrell, and A. M. Campbell, “Theory and experiment testing flux-line cutting physics,” *Supercond. Sci. Technol.* **24**, 062002 (2011).
- [29] J.R. Clem and A. Perez-Gonzalez, “Flux-line-cutting and flux-pinning losses in type-II superconductors in rotating magnetic fields,” *Phys. Rev. B* **30**, 5041 (1984).
- [30] E. H. Brandt and G. P. Mikitik, “Unusual critical states in type-II superconductors,” *Phys. Rev. B* **76** (2007).
- [31] C. Romero-Salazar and F. Pérez-Rodríguez, “Elliptic flux-line-cutting critical-state model,” *Appl. Phys. Lett.* **83**, 5256 (2003).
- [32] V. Chepikov, N. Mineev, P. Degtyarenko, S. Lee, V. Petrykin, A. Ovcharov, A. Vasiliev, A. Kaul, V. Amelichev, A. Kamenev, A. Molodyk, and S. Samoilenkov, “Introduction of BaSnO_3 and BaZrO_3 artificial pinning centres into 2G HTS wires based on PLD GdBCO films. Phase I of the industrial R&D programme at SuperOx,” *Supercond. Sci. Technol.* **30** (2017).
- [33] Y. Iijima, Y. Adachi, S. Fujita, M. Igarashi, K. Kakimoto, M. Ohsugi, N. Nakamura, S. Hanyu, R. Kikutake, M. Daibo, M. Nagata, F. Tateno, and M. Itoh, “Development for mass production of homogeneous RE123 coated conductors by hot-wall PLD process on IBAD template technique,” *IEEE Trans. Appl. Supercond.* **25** (2015).
- [34] J. Lee, B. Mean, T. Kim, Y. Kim, K. Cheon, T. Kim, D. Park, D. Song, H. Kim, W. Chung, H. Lee, and S. Moon, “Vision inspection methods for uniformity enhancement in long-length 2g hts wire production,” *IEEE Trans. Appl. Supercond.* **24** (2014).
- [35] L. Rossi, X. Hu, F. Kametani, D. Abraimov, A. Polyanskii, J. Jaroszynski, and DC. Larbalestier, “Sample and length-dependent variability of 77 and 4.2 K properties in nominally identical RE123 coated conductors,” *Supercond. Sci. Technol.* **29** (2016).
- [36] A. Xu, Y. Zhang, M. Gharahcheshmeh, L. Delgado, N. Khatri, Y. Liu, E. Galstyan, and V. Selvamanickam, “Relevant pinning for ab-plane $J(c)$ enhancement of MOCVD REBCO coated conductors,” *IEEE Trans. Appl. Supercond.* **27** (2017).
- [37] JX. Lin, XM. Liu, CW. Cui, CY. Bai, YM. Lu, F. Fan, YQ. Guo, ZY. Liu, and CB. Cai, “A review of thickness-induced evolutions of microstructure and superconducting performance of

- REBa₂Cu₃O₇-delta coated conductor,” *Advances in Manufacturing*. **5**, 165–176 (2017).
- [38] S. Miura, Y. Tsuchiya, Y. Yoshida, Y. Ichino, S. Awaji, K. Matsumoto, A. Ibi, and T. Izumi, “Strong flux pinning at 4.2 K in SmBa₂Cu₃O_y coated conductors with BaHfO₃ nanorods controlled by low growth temperature,” *Supercond. Sci. Technol.* **30** (2017).
- [39] N. Ayai, S. Kobayashi, M. Kikuchi, T. Ishida, J. Fujikami, K. Yamazaki, S. Yamade, K. Tatamidani, K. Hayashi, K. Sato, H. Kitaguchi, H. Kumakura, K. Osamura, J. Shimoyama, H. Kamijyo, and Y. Fukumoto, “Progress in performance of DI-BSCCO family,” *Physica C-Superc. and its apl.* **468**, 1747–1752 (2008).
- [40] A. Goyal, DP. Norton, DM. Kroeger, DK. Christen, M. Paranthaman, ED. Specht, JD. Budai, Q. He, B. Saffian, FA. List, DF. Lee, E. Hatfield, PM. Martin, CE. Klabunde, J. Mathis, and C. Park, “Conductors with controlled grain boundaries: An approach to the next generation, high temperature superconducting wire,” *J. Mar. Res.* **12**, 2924–2940 (1997).
- [41] I. Pallecchi, M. Eisterer A. Malagoli, and M. Putti, “Application potential of Fe-based superconductors,” *Supercond. Sci. Technol.* **28** (2015).
- [42] W. Yi, Q. Wu, and LL. Sun, “Superconductivities of pressurized iron pnictide superconductors,” *Acta Physica Sinica.* **66** (2017).
- [43] YH. Ma, QC. Ji, KK. Hu, B. Gao, W. Li, G. Mu, and XM. Xie, “Strong anisotropy effect in an iron-based superconductor CaFe0: 882Co0: 118AsF,” *Supercond. Sci. Technol.* **30** (2017).
- [44] J. Hecher, S. Ishida, D. Song, H. Ogino, A. Iyo, H. Eisaki, M. Nakajima, D. Kagerbauer, and M. Eisterer, “Direct observation of in-plane anisotropy of the superconducting critical current density in Ba(Fe_{1-x}Cox)(2)As-2 crystals,” *Phys. Rev. B* **97** (2018).
- [45] A high-temperature superconducting (HTS) wire critical current database. https://figshare.com/collections/A_high_temperature_superconducting_HTS_wire_critical_current_database/2861821.
- [46] E. Pardo, M. Vojenciak, F. Gomory, and J. Souc, “Low-magnetic-field dependence and anisotropy of the critical current density in coated conductors,” *Supercond. Sci. Technol.* **24**, 10 (2011).
- [47] VMR. Zermeno, S. Quaiyum, and F. Grilli, “Open-source codes for computing the critical current of superconducting devices,” *IEEE Trans. Appl. Supercond.* **26** (2016).
- [48] E. Pardo and M. Kapolka, “3D computation of non-linear eddy currents: variational method and superconducting cubic bulk,” *J. Comput. Phys.* (2017).

- [49] A. Badía-Majós and C. López, “Modelling current voltage characteristics of practical superconductors,” *Supercond. Sci. Technol.* **28**, 024003 (2015).
- [50] E. Pardo and M. Kapolka, “3D magnetization currents, magnetization loop, and saturation field in superconducting rectangular prisms,” *Supercond. Sci. Technol.* **30**, 11 (2017).
- [51] C. P. Bean, “Magnetization of hard superconductors,” *Phys. Rev. Lett.* **8**, 250–253 (1962).
- [52] H. London, “Alternating current losses in superconductors of the second kind,” *Phys. Letters* **6**, 162–165 (1963).
- [53] A. Perezgonzalez and J. R. Clem, “Magnetic response of type-II superconductors subjected to large-amplitude parallel magnetic-fields varying in both magnitude and direction,” *J. Appl. Phys.* **58**, 4326–4335 (1985).
- [54] A. Badía-Majós and C. López, “Electromagnetics close beyond the critical state: thermodynamic prospect,” *Supercond. Sci. Technol.* **25**, 104004 (2012).
- [55] O. Ciftja, “Coulomb self-energy of a uniformly charged three-dimensional cube,” *Physics Letters A* **375**, 766–767 (2011).
- [56] O. Ciftja, “Coulomb self-energy and electrostatic potential of a uniformly charged square in two dimensions,” *Physics Letters A* **374**, 981–983 (2010).